

1 **Formulation of a new explicit tidal scheme in revised LICOM2.0**

2 Jiangbo Jin^{1,2}, Run Guo^{1,3}, Minghua Zhang⁴, Guangqing Zhou¹, Qingcun Zeng^{1,*}

3 *¹International Center for Climate and Environment Sciences, Institute of Atmospheric Physics,*
4 *Chinese Academy of Sciences, Beijing 100029, China*

5 *²State Key Laboratory of Satellite Ocean Environment Dynamics, Second Institute of*
6 *Oceanography, Ministry of Natural Resources, Hangzhou 310012, China*

7 *³College of Earth and Planetary Sciences, University of Chinese Academy of Sciences, Beijing*
8 *100049, China*

9 *⁴School of Marine and Atmospheric Sciences, Stony Brook University, Stony Brook, New York,*
10 *USA*

11
12
13
14
15
16 *Submitted to Geoscientific Model Development*

17
18
19 **Corresponding author, E-mail: zqc@mail.iap.ac.cn*

20

ABSTRACT

21
22
23
24
25
26
27
28
29
30
31
32
33
34
35
36
37

Tides play an important role in ocean energy transfer and mixing, and provide major energy for maintaining thermohaline circulation. This study proposes a new explicit tidal scheme and assesses its performance in a global ocean model. Instead of using empirical specifications of tidal amplitudes and frequencies, the new scheme directly uses the positions of the Moon and Sun in a global ocean model to incorporate tides. Compared with the traditional method that has specified tidal constituents, the new scheme can better simulate the diurnal and spatial characteristics of the tidal potential of spring and neap tides as well as the spatial patterns and magnitudes of major tidal constituents (K1 and M2). It significantly reduces the total errors of eight tidal constituents (with the exception of N2 and Q1) in the traditional explicit tidal scheme, in which the total errors of K1 and M2 are reduced by 21.85% and 32.13%, respectively. Relative to the control simulation without tides, both the new and traditional tidal schemes can lead to better dynamic sea level (DSL) simulation in the North Atlantic, reducing significant negative biases in this region. The new tidal scheme also shows smaller positive bias than the traditional scheme in the Southern Ocean. The new scheme is suited to calculate regional distributions of sea level height in addition to tidal mixing.

38 **1. Introduction**

39 Diapycnal mixing plays a crucial role in the interior stratification of global oceans and
40 meridional overturning circulation. To sustain the mixing, a continuous supply of mechanical
41 energy is needed (Huang 1999; MacKinnon 2013). It has been suggested that the breaking of
42 internal tides is a major contribution to diapycnal mixing in deep seas (Wang et al., 2017),
43 whereas the breaking of internal waves generated by surface wind is a major source within the
44 upper ocean (Wunsch and Ferrari 2004). Through the analysis of observational data and
45 numerical model simulations, previous studies have shown that tides can provide about 1TW of
46 mechanical energy for maintaining the thermohaline circulation, accounting for about half of the
47 total mechanical energy (Egbert and Ray, 2003; Jayne and Laurent, 2001). Local strong tidal
48 mixing also affects ocean circulations on a basin scale. For instance, tidal mixing in both the
49 Luzon Strait and South China Sea has a pronounced impact on water mass properties and, in the
50 South China Sea, has intermediate–deep layer circulation features (Wang et al., 2017). Due to
51 interactions with sea ice, tidal mixing in the Arctic seas could modify the salinity budget, which
52 further affects the deep thermohaline circulation in the North Atlantic (Postlethwaite et al., 2011).
53 Therefore, it is necessary to fully consider the effects of tidal processes in state-of-the-art ocean
54 models.

55 Tides were omitted in the early ocean general circulation models (OGCMs) in which the
56 “rigid-lid” approximation is applied to increase the integration time steps of the barotropic
57 equation for computational efficiency, which filtered out the gravity waves including the tides.

58 Free surface methods were later introduced to ocean models (e.g., Zhang and Liang, 1989;
59 Killworth et al., 1991; Zhang and Endoh, 1992), but tides were often neglected since the focus of
60 many studies has been on the variations in large-scale ocean general circulations on much longer
61 time scales than tides. With the development of theories of ocean general circulations and the
62 recognition of the importance of tides on large-scale circulations, the effects of tides have begun
63 to be considered in OGCMs in the last twenty years.

64 The tidal processes are typically incorporated into OGCMs in two different ways. One is in
65 an implicit form and the other is in an explicit form. The implicit form uses an indirect
66 parameterization scheme that does not simulate the tides themselves (Laurent et al. 2002). It
67 enhances mixing, especially for deep seas and coastal areas, to represent the tidal effects. This
68 type of mixing scheme was first applied in a coarse-resolution OGCM by Simmons et al. (2004),
69 and their results show that the biases of ocean temperature and salinity are substantially smaller.
70 Saenko and Merryfield (2005) reported that this type of parameterization scheme contributes to
71 the amplification of bottom-water circulation especially for the Antarctic Circumpolar Current
72 and deep-sea stratification. Yu et al. (2017) pointed out that the tidal mixing scheme has a
73 significant effect on the simulation of the Atlantic meridional overturning circulation (AMOC)
74 intensity in OGCM. This parameterization type is mainly used for internal-tide generation, in
75 which the resultant vertical mixing is ad hoc, with an arbitrarily prescribed exponential vertical
76 decay (Melet et al., 2013).

77 The explicit form incorporates the tidal forcing into the barotropic equation of free-surface
78 OGCMs. The typical tidal forcing consists of four primary diurnal (K1, O1, P1 and Q1) and four
79 primary semidiurnal (M2, S2, N2 and K2) constituents. Each of the constituents is determined by
80 a prescribed amplitude, frequency and phase (Griffies et al. 2009). The explicit tidal forcing has
81 been implemented in several OGCMs in recent decades (Thomas et al., 2001; Zhou et al., 2002;
82 Schiller, 2004; Schiller and Fiedler, 2007; Müller et al., 2010). Arbic et al. (2010) reported the
83 first explicit incorporation of tides into an eddy-resolving OGCM that led to a drastic
84 improvement in the interaction between tides and mesoscale eddies.

85 The purpose of this study is to propose a new explicit tidal scheme in a CMIP6 class of
86 OGCMs (Phase 6 of the Coupled Model Intercomparison Project) and assess its performance.
87 The scheme is directly based on the actual position of the Sun and Moon relative to the Earth and
88 calculates precise gravitational tidal forcing instead of applying the empirical constants of tidal
89 amplitudes and frequencies.

90 The structure of this paper is as follows: the new explicit tidal scheme is introduced in
91 section 2. The model configuration, numerical experiment design and data used in this study are
92 described in section 3. Section 4 presents the results of the numerical experiment. Section 5
93 contains a summary and discussion.

94 **2. The new explicit tidal forcing**

95 Tidal forcing is mainly the result of the combination of the gravitational pull exerted by the
96 Moon and Sun and inertial centrifugal forces generated by the Earth's rotation. First, we only

97 take the Moon as an example for simplicity (Fig. 1); the vertical tidal force can be ignored,
 98 which is far less than the gravity, and is part of the force in the hydrostatic balance. Assuming
 99 that the Earth is a rigid body, the horizontal tide-generating force is (Cartwright, 1999; Boon,
 100 2004):

$$F_{tide,m} = \frac{GM_m}{L^2} \sin(\theta_m + r) - \frac{GM_m}{D_m^2} \sin \theta_m \quad (1)$$

101 where $F_{tide,m}$ represents the horizontal tide-generating force generated by the moon, the first
 102 term on the right-hand side is the horizontal gravitational force at the surface, and the second
 103 term is the horizontal gravitational force at the center that should be equal to the inertial
 104 centrifugal force. G is the universal gravitation constant which can also be denoted as $g \frac{a^2}{E}$,
 105 (where g is gravitational acceleration, E is the mass of the Earth, and a is the radius of the Earth),
 106 M_m is the mass of the moon, r is the angle between the Moon pointing to the center of the Earth
 107 and point X, L and θ_m are is the distance and zenith angle of the Moon and an arbitrary position
 108 X on the Earth (Fig. 1). Therefore, $F_{tide,m}$ can be considered the deviation of the horizontal
 109 gravitational force at the surface from that at the center of the Earth.

110 According to analytic geometry and the law of cosines, we can obtain:

$$\sin(\theta_m + r) = \frac{D_m \sin \theta_m}{L} \quad (2)$$

$$L^2 = D_m^2 + a^2 - 2aD_m \cos \theta_m \quad (3)$$

111 Where, D_m is Earth-Moon distance. Based on the above three equations, equation (1) can be
 112 written as (see Supplement):

$$F_{tide,m} \approx -\frac{3}{2} \frac{M_m}{E} \left(\frac{a}{D_m} \right)^3 g \sin 2\theta_m \quad (4)$$

113 To compare with the traditional explicit tidal forcing formula of the eight most important
 114 constituents of the diurnal and semidiurnal tides, the instantaneous tidal height (tidal potential)
 115 caused by moon due to equilibrium tides is diagnosed by the spatial integration of equation (4):

$$\eta_{tide,m} = \int_{\Theta}^{\theta_m} (F_{tide,m} \cdot a) d\theta_m \quad (5)$$

116 Where, Θ is the zenith angle of the zero potential energy surface. With the global total tidal
 117 height at zero, $\cos^2 \Theta = 1/3$. Therefore, the instantaneous tidal height is:

$$\eta_{tide,m} = \frac{M_m}{E} \frac{a^4}{D_m^3} \frac{h}{2} (3\cos^2 \theta_m - 1) \quad (6)$$

118 where the love number h is introduced to represent the reduction in tidal forcing caused by the
 119 deformation of the solid Earth. It is usually set equal to 0.7 (Wahr, 1981; Griffies 2004), which is
 120 adopted here.

121 Therefore, the tidal potential after taking into account tidal forcing due to both the Moon
 122 and Sun is as follows:

$$\eta_{tide} = \frac{M_m}{E} \frac{a^4}{D_m^3} \frac{h}{2} (3\cos^2 \theta_m - 1) + \frac{M_s}{E} \frac{a^4}{D_s^3} \frac{h}{2} (3\cos^2 \theta_s - 1) \quad (7)$$

123 The zenith angle θ_m is calculated as follows:

$$\cos \theta_m = \sin \varphi \sin \varphi_m + \cos \varphi \cos \varphi_m \cos(\lambda_m - \lambda) T_{\text{mm}} \quad (8)$$

$$T_{\text{mm}} = \begin{cases} \lambda_{\text{mm}} - \lambda, & (\lambda_{\text{mm}} - \lambda) \in [0, \pi] \\ \lambda_{\text{mm}} - \lambda + 2\pi, & (\lambda_{\text{mm}} - \lambda) \notin [0, \pi] \end{cases} \quad (9)$$

124 where φ and λ are the latitude and longitude of the position X on the Earth, respectively; φ_m and
 125 λ_m are the latitude and longitude of the projection point of the Moon on the Earth, respectively,
 126 and are both functions of universal time (Montenbruck and Gill, 2000). The zenith angle θ_s is
 127 similarly calculated.

128 Finally, explicit tidal forcing is introduced into the equation of barotropic mode motion:

$$\frac{\partial \vec{V}}{\partial t} = -\frac{1}{\rho_0} \nabla_h p_{as} - g' \nabla_h (\alpha \eta - \eta_{tide}) + \bar{P} + f \vec{k} \times \vec{V} + \tau_{tide} \quad (109)$$

129 where \vec{V} is the barotropic velocity, $\nabla_h = (\partial/\partial x, \partial/\partial y)$; p_{as} is the sea surface air pressure; $g' =$
130 $g\rho/\rho_0$ and $\alpha = 0.948$ represent the self-attraction of the Earth and the correction generated by
131 full self-attraction and loading (SAL) (Hendershott, 1972), which refers to the redistribution of
132 the sea surface height between the Earth and the ocean due to the existence of tide-generating
133 potential. SAL treatment is a scalar approximation in order to make the calculation feasible.
134 Currently, many tidal studies have applied SAL treatment (Simmons et al., 2004; Schiller and
135 Fiedler, 2007; Griffies 2008; Arbic et al., 2010). η is the sea surface fluctuation and η_{tide} is the
136 instantaneous sea surface height due to equilibrium tides. \bar{P} represents the force from the
137 vertically integrated baroclinicity in the ocean columns, and the last term on the right side of the
138 equation (10) is the vertically integrated Coriolis force. Introduction of tidal forcing leads to
139 disrupt the dynamical balance of the ocean circulation in the original OGCM (Sakamoto et al.,
140 2013), and Arbic et al (2010) pointed out the global tidal simulations must include parameterized
141 topographic wave drag in order to accurately simulate the tides, we added a drag term τ_{tide} , in
142 barotropic equation, including parameterized internal wave drag due to the oscillating flow over
143 the topography and the wave drag term due to the undulation of the sea surface (Jayne and
144 Laurent, 2001; Simmons et al. 2004; Schiller and Fiedler, 2007). ~~τ_{tide} is a drag term, and~~
145 ~~includes parameterized internal wave drag due to the oscillating flow over the topography and~~
146 ~~the wave drag term due to the undulation of the sea surface (Jayne and Laurent, 2001; Simmons~~
147 ~~et al. 2004; Schiller and Fiedler, 2007).~~

148 **3. Model description, numerical experimental design and data**

149 **3.1 Model**

150 The OGCM in this study is the second revised version of the LASG/IAP's (State Key
151 Laboratory of Numerical Modeling for Atmospheric Sciences and Geophysical Fluid
152 Dynamics/Institute of Atmospheric Physics) climate system ocean model (LICOM2.0) (Liu et al.,
153 2012; Dong et al., 2021), which adopts the free surface scheme in η -coordinate models and offers
154 the opportunity to explicitly resolve tides. The model domain is located between 78.5°S and
155 87.5°N with a 1° zonal resolution. The meridional resolution is refined to 0.5° between 10°S and
156 10°N and is increased gradually from 0.5° to 1° between 10° and 20°. There are 30 levels in the
157 vertical direction with 10m per layer in the upper 150m. Based on the original version of
158 LICOM2.0, key modifications have been made: (1) a new sea surface salinity boundary
159 condition was introduced that is based on the physical process of air–sea flux exchange at the
160 actual sea–air interface (Jin et al., 2017); (2) intra-daily air–sea interactions are resolved by
161 coupling the atmospheric and oceanic model components once every 2h; and (3) a new
162 formulation of the turbulent air–sea fluxes (Fairall et al., 2003) was introduced. The model has
163 been used as the ocean component model of the Chinese Academy of Sciences Earth System
164 Model (CAS-ESM 2.0) in its CMIP6 simulations (Zhang et al., 2020; Dong et al., 2021; Jin et al.,
165 2021).

166 **3.2 Numerical experimental design**

167 To investigate the effect of tidal processes on the simulation of the ocean climate, three sets
168 of experiments were conducted in the present study. The control experiment used the default
169 LICOM2.0 without tidal forcing (denoted as “CTRL” hereafter); Exp1 used the traditional
170 explicit tidal forcing formula of the eight most important constituents of the diurnal and
171 semidiurnal tides proposed by Griffies et al. (2009), and Exp2 used the new tidal forcing scheme.

172 For the control experiment, the Coordinated Ocean-ice Reference Experiments-I (CORE I)
173 protocol proposed by Griffies et al. (2009) was employed, and the repeating annual cycle of
174 climate atmospheric forcing from Large and Yeager (2004) was used. The model was firstly
175 spun up for 300 years in order to reach a quasi-equilibrium state. All three experiments started
176 from the quasi-equilibrium state (300th year) of the spin-up experiment and are integrated for 50
177 years under the same CORE I forcing fields. The diapycnal mixing of Laurent et al. (2002) and
178 Simmons et al. (2004) was also applied to the baroclinic momentum and tracer equations. The
179 hourly output of sea surface height in the last 10 years of the two tidal experiments was used to
180 conduct the harmonic analysis and obtain the spatial information of tidal constituents.

181 **3.3 Data**

182 TPXO9v2 is the assimilated data from a hydrodynamic model of the barotropic tides
183 constrained by a satellite altimetry (Egbert and Erofeeva, 2002). To verify the effect of the two
184 tidal schemes for high tidal amplitude regions, we also used two tidal stations, Yakutat (59.54°N,
185 139.73°W) and the Diego Ramirez Islands (56.56°S, 68.67°W), where the spectrum analysis was
186 carried out. The station observations are from the sea level Data Assembly Center (DAC) of the

187 World Ocean Circulation Experiment (WOCE) (Ponchaut et al., 2001). The data obtained from
188 the Archiving, Validation and Interpretation of Satellite Oceanographic data (AVISO)
189 (Schneider et al., 2013) are used in the observation of the dynamic sea level (DSL).

190 **4. Result**

191 **4.1 Tidal forcing**

192 Tides include spring tides, which are on the same line with the Sun, the Earth and the Moon,
193 and neap tides, which are when the Sun, the Earth and the Moon are not aligned. Figure 2 and
194 Figure 3 show the spatial distributions of spring and neap tidal height η_{tide} calculated by the two
195 tidal schemes. As expected, the two types of tides in Exp1 and Exp2 both have significant
196 diurnal variations and exhibit a phase shift from east to west (Fig. 2). Both experiments
197 simulated similar positions of the positive centers for spring tides, which are consistent with the
198 overlap of the projected positions of the Moon and the Sun. It is important to note that the
199 negative regions of the spring tide simulated in Exp2 exhibit large non-closed circular bands,
200 which represents the elliptic model of the equilibrium tide theory (Schwiderski, 1980), and this is
201 absent in Exp1 where the traditional explicit eight tidal constituents scheme is used.

202 There are pronounced differences in neap tides between Exp1 and Exp2 (Fig. 3). The neap
203 tide simulated in Exp2 shows a larger meridional variation. The positive regions are mainly
204 concentrated in the middle and low latitudes. The negative regions are mainly concentrated in
205 the high latitudes of the two hemispheres, because the projection positions of the Sun and Moon

206 are located in the middle and low latitudes, resulting in the relatively weaker tidal potential in the
207 high latitudes farther away from the projection position, which is consistent with the results of
208 Gill (2015).which is due to less tidal forcing in the high latitudes compared to the middle and
209 low latitudes. This pattern of neap tide in Exp2 indicates that the projection positions of both the
210 Sun and Moon are located in the middle and low latitudes, which is consistent with the results of
211 Gill (2015). However, Exp1 presents a larger zonal variation (positive-negative-positive-negative
212 pattern), and the negative regions are concentrated in the middle and low latitudes rather than the
213 high latitudes, and the tidal potential in the polar regions is even higher than the negative regions
214 in low latitudes, which means that the projection position of the sun is incorrect, locating at high
215 latitudes rather than at low latitudes. Therefore, the new tidal scheme can better represent the
216 position of the Sun compared to the traditional scheme,which implies that the projection position
217 of the Sun is located in the high latitudes. The different distributions of neap tides between Exp1
218 and Exp2 indicate that the new tidal formulation can better represent the position of the Sun
219 compared to the traditional scheme.

220 **4.2 Tidal constituents**

221 The harmonic analysis of the hourly sea surface height data simulated by the two tidal
222 schemes is carried out in order to obtain the amplitude and phase of each major tidal constituent.
223 TPXO9v2 is used as the observed data (Egbert and Erofeeva, 2002). In this study, we mainly
224 focus on the amplitudes and phases of the two largest constituents among the eight tidal
225 constituents, including a full diurnal constituent of K1 and a half-diurnal constituent of M2. To

226 quantitatively compare the simulations of tidal constituents by the two schemes, we calculated
227 the mean square error following Shriver et al. (2012):

$$total\ error^2 = \left[\frac{1}{2} (A_{model} - A_{TPXO})^2 \right] + [A_{model} A_{TPXO} (1 - \cos(\phi_{model} - \phi_{TPXO}))] \quad (11)$$

228 where A_{model} and A_{TPXO} are simulated and observed amplitudes, respectively, and ϕ_{model} and
229 ϕ_{TPXO} are simulated and observed phases, respectively. The total errors in each tidal constituent
230 can be divided into amplitude error and amplitude-weighted phase error (phase error)~~phase error~~;
231 the former is the first term on the right side of equation (11), and the latter is the second term on
232 the right side of equation (11).

233 Figure 4 shows the respective amplitudes and phases of K1 for the observation, Exp1, and
234 Exp2, the total errors for the two experiments against the observation, and the difference in the
235 total errors between the two experiments. The amplitudes and phases of K1 simulated in both
236 Exp1 and Exp2 are similar to the observation (Fig. 4a–4c). The large values of the amplitudes of
237 K1 are located in the North Pacific Ocean, Indonesia, Ross Sea and Weddell Sea. However,
238 Exp1 simulated a larger amplitude of K1, and the extent of the large amplitude is too excessive,
239 especially for the North Pacific Ocean and Southern Ocean, compared to the extent of the large
240 amplitude in the observation and Exp2, which is consistent with the results of Yu et al. (2016).
241 The simulated amplitude of K1 by Exp2 is significantly improved and closer to the observation.
242 The global mean values of K1 are 11.58cm, 14.74cm and 10.50cm for the observation, Exp1 and
243 Exp2, respectively.

244 The total error patterns of K1 in Exp1 and Exp2 show ~~a~~ similar distributions (Fig. 4d and
245 4e); large values are located in the Southern Ocean and the North Pacific. The total error of K1
246 in Exp2 is smaller than in Exp1 in most regions except for the Arabian Sea, especially for the
247 Southern Ocean, the North Pacific and the eastern equatorial Pacific (Fig. 4f). The global mean
248 total errors of the K1 in Exp1 and Exp2 are 7.43cm and 6.28cm, respectively. According to
249 formula (11), the total error of K1 is divided into amplitude error and phase error (Fig. 5).
250 Compared with Exp1, the amplitude error of K1 is significantly improved in most regions,
251 especially for the large amplitude of K1 regions, which is the main reason for the smaller total
252 error of K1 in Exp2, although the phase error is also slightly reduced; this suggests that the new
253 tidal scheme leads to a better simulation of the amplitude and phase of K1, especially for the
254 amplitude simulation. The global mean of the amplitude errors in Exp1 and Exp2 are 4.97cm and
255 3.73cm, respectively, and the corresponding phase errors in both experiments are 5.52cm and
256 5.06cm, respectively.

257 M2 is known to be the largest tidal constituent (Griffies et al. 2009). Figure 6 shows the
258 respective amplitudes and phases of M2 for the observation, Exp1, and Exp2, as well as the total
259 errors for the two experiments against the observation and the difference in the total errors
260 between the two experiments. Both Exp1 and Exp2 can reasonably simulate the overall spatial
261 distribution patterns of M2's amplitude and phase (Fig. 6a–6c). The maximum values of the
262 amplitude are located in the Bay of Alaska, the eastern equatorial Pacific, Sman sea and the
263 North Atlantic. The amplitudes of M2 simulated in both Exp1 and Exp2 are larger than the

264 observation, especially for Ross Sea and Weddell Sea, though Exp2 exhibits some alleviation of
265 the bias when compared to Exp1. The global mean values of M2 are 33.30cm, 42.76cm and
266 38.29cm for the observation, Exp1 and Exp2, respectively.

267 The total error patterns of M2 in Exp1 and Exp2 also show similar features (Fig. 6d and 6e);
268 the large values are located in the large amplitude of M2 regions, noting the smaller magnitude
269 of the total error of M2 in Exp2 relative to Exp1 in most regions. The global mean of total error
270 in Exp2 (24.42cm) is obviously lower than in Exp1 (37.21cm). In addition, the amplitude error
271 and the phase error of M2 in Exp2 are both improved, the global mean of amplitude errors in
272 Exp1 and Exp2 are 14.77cm and 12.86cm, respectively, and the corresponding phase errors in
273 Exp1 and Exp2 are 34.16cm and 20.76cm, respectively. Inconsistent with K1, the smaller total
274 error of M2 in Exp2 relative to Exp1 is mainly the result of the phase error; in particular, the
275 phase errors of Exp2 are almost eliminated in the Indian Ocean and the Atlantic Ocean (Fig. 7).
276 This indicates the new tidal scheme results in the better simulation of M2, especially for the
277 phase simulation. Compared with Exp1, the total errors of K1 and M2 in Exp2 are reduced by
278 21.85% and 32.13% respectively.

279 Furthermore, we also investigate the amplitudes and total errors of the remaining six tidal
280 constituents (O1, P1, Q1, S2, N2 and K2) simulated using two schemes. For amplitudes, the
281 global means of the three constituents (O1, P1 and K2) in Exp2 are closer to the observed values
282 relative to Exp1. The global mean observed values for the O1, P1, Q1, S2, N2 and K2 are
283 8.34cm, 3.62cm, 1.76cm, 13.35cm, 7.08cm and 3.75cm, respectively, and the corresponding

284 values in Exp1 (Exp2) are 10.59cm (9.79cm), 13.49cm (9.47cm), 1.62cm (2.19cm), 12.45cm
285 (9.85cm), 7.74cm (9.79cm) and 10.89cm (7.33cm), respectively (Table 1). For the total errors,
286 the global mean total errors for the remaining six constituents in Exp2 (with the exception of Q1
287 and N2) are smaller than those in Exp1, and the global mean total errors of the remaining six
288 constituents in Exp1 (Exp2) are 8.89cm (5.34cm), 9.53cm (6.26cm), 1.29cm (1.47cm), 11.26cm
289 (9.40cm), 5.84cm (6.76cm) and 10.32cm (6.55cm), respectively. Compared to Exp1, the
290 improved total errors of O1 and S2 in Exp2 are mainly the result of the smaller phase errors, and
291 the improvement of the total error of P1 in Exp2 is predominantly due to the lower amplitude
292 error. The global mean amplitude errors of O1, P1, S2, and K2 in Exp1 (Exp2) are 3.28cm
293 (3.16cm), 9.18cm (5.58cm), 5.11cm (5.68cm) and 6.50cm (3.72cm), respectively, and the
294 corresponding phase errors are 8.26cm (4.30cm), 2.57cm (2.84cm), 10.04cm (7.49cm) and
295 8.01cm (5.39cm), respectively (Table 1). The above results indicate that the new formulation of
296 the tidal scheme can better simulate more constituents of tides relative to the traditional method
297 of eight tidal constituents with empirical amplitudes and frequencies.

298 To further evaluate the simulation of the eight tidal constituents by using the two tidal
299 schemes, we also made a spectrum analysis at the Diego Ramirez Islands (56.56°S, 68.67°W)
300 and Yakutat (59.54°N, 139.73°W) tidal stations, which are located in regions with large tidal
301 amplitudes (Fig. 8). Both Exp1 and Exp2 can reasonably reproduce the amplitudes and
302 frequencies of the eight main tidal constituents at the Diego Ramirez Islands and Yakutat stations,
303 although most of the simulated amplitudes in Exp1 are much larger than the observed data. The

304 larger amplitude biases of the eight main tidal constituents at both stations (except for the Q1
305 constituent at the Diego Ramirez station) are all significantly improved in Exp2 (Table 2). For
306 instance, the amplitude of M2 in Exp1 at the Yakutat station is 141.58cm, and it is reduced to
307 130.65cm in Exp2, which is closer to the observed data (101.24cm). The amplitude of K1 in
308 Exp1 at the Diego Ramirez station is 26.13cm, and it is reduced to 17.59cm in Exp2, which is
309 closer to the observed data (18.82cm). On the basis of these preliminary evaluations, compared
310 to the traditional explicit eight tidal constituents scheme, the new tidal scheme can better
311 reproduce the spatial patterns of the amplitude of tidal constituents and tidal forcing, especially
312 for the magnitude of the amplitude. Furthermore, we conduct two experiments (one using
313 traditional tidal scheme, the other applying new tidal scheme) by also adopting the practical
314 scheme following Sakamoto et al. (2013), we found the errors (including the phase error and
315 total error) of all the eight tidal constituents of the experiment using the new tidal scheme are
316 less than that applies the tradition tidal scheme (Table R1).

317 **4.3 Dynamic sea level (DSL)**

318 Figure 9 shows the spatial distributions of DSL that is defined as the sea level associated
319 with the fluid dynamic state of the ocean (Griffies and Greatbatch, 2012; Griffies et al., 2016) for
320 the observation, CTRL and the bias in CTRL, Exp1 and Exp2 relative to the observations as well
321 as the difference between Exp2 and Exp1. The observation is obtained from the Archiving,
322 Validation and Interpretation of Satellite Oceanographic data (AVISO) (Schneider et al., 2013).
323 The DSL simulated by CTRL shows a low DSL located in the Labrador Sea, the Nordic Seas and

324 the Southern Ocean, and a high DSL in the tropical and subtropical Pacific and Indian Oceans
325 (Fig. 9b), which is consistent with the observed data (Fig. 9a). Therefore, the ocean model,
326 LICOM2.0, without a tidal process can reproduce the basic pattern of DSL, but large biases also
327 exist (Fig. 9c); there is a dipole pattern bias located across the Antarctic Circumpolar Circulation
328 (negative bias to the north and positive bias to the south), a striking negative bias in the North
329 Atlantic and a slightly positive bias in the western equatorial Pacific.

330 The DSL in both Exp1 and Exp2 are improved and the striking negative bias for the North
331 Atlantic is reduced (Fig. 9d and 9e), which can be attributed to the improvement of the path of
332 the North Atlantic Gulf Stream due to the effects of tides, as pointed out by Müller et al. (2010).
333 There are some significant differences between Exp1 and Exp2. Compared to Exp1, Exp2
334 exhibits a striking latitudinal distribution feature (Fig. 9f), which shows a decreasing spatial
335 pattern from the equator to the poles, with positive values in the tropic region and a negative
336 pattern in high latitudes. This is because Exp2, in applying the new formulation of the tidal
337 scheme, can ~~consider~~better represent the ~~projection~~ positions of both the Sun and Moon relative
338 to Exp1. ~~Therefore, e~~Compared to Exp1, the positive bias in the Southern Ocean simulated by
339 CTRL is improved in Exp2, as exhibited by the negative difference between Exp2 and Exp1 at
340 high latitudes. This is because Exp2 applying the new formulation of the tidal scheme can
341 reasonably consider the positions of both the Sun and Moon relative to Exp1, which makes the
342 higher DSL in low latitude compared to that in high latitude due to the effect of gravity.

343 5. Summary

344 In this paper, a new explicit tidal scheme is introduced to a global ocean model. The scheme
345 uses the positional characteristics of the Moon and the Sun to calculate the tides directly instead
346 of applying empirical specifications, such as the amplitudes and frequencies of tides, which were
347 used in traditional methods. The new tidal scheme has some unique advantages: It can accurately
348 provide instantaneous tidal potentials, since both astronomers and oceanographers have well
349 established models for determining the exact position of the sun and the moon by Julian and for
350 calculating the instantaneous tidal potential by their projected positions. Traditional tidal scheme
351 does not guarantee the correct transient tidal potential at any given time, as described in Section
352 4.1. Traditional method does not cover all tidal constituents, so it is more suitable to study only
353 one specific tidal constituent rather than the full real tidal process in the OGCM. Besides, in the
354 traditional scheme, the tidal potential is introduced in the form of sine wave, so that the climate
355 state of tidal potential is zero at any position. The new tidal method does not impose this
356 particular time variation.

357 Compared with the traditional explicit eight tidal constituents scheme, we found that the new
358 tidal scheme can better simulate the spatial characteristics of spring and neap tides. It
359 significantly reduces the biases of larger amplitudes in the traditional explicit tidal scheme, and
360 better reproduces the spatial patterns of tidal constituents than the traditional method. In theory,
361 this scheme is also better suited than the traditional method to simulate sea level height at
362 regional scales which may not all be captured by the small number of prescribed
363 constituents~~modes~~.

364 Furthermore, we study the total errors of the eight tidal constituents, including amplitude
365 errors and phase errors. The total errors of the eight tidal constituents simulated by the new tidal
366 scheme, with the exception of N2 and Q1, are all smaller than those simulated by the traditional
367 method. Compared to the traditional method, the improved total errors of M2, O1 and S2
368 simulated by the new tidal scheme are mainly the result of the better phase simulation (the
369 smaller phase errors); the reduction in the total errors of K1 and P1 are predominantly due to the
370 improvement in the amplitude simulation (with fewer amplitude errors); and the smaller total
371 error of K2 is associated with both the improvements in the amplitude and phase simulation
372 (both the smaller phase and amplitude errors).

373 The influence of tidal forcing on the simulation of DSL is also investigated. We found both
374 tidal schemes can significantly improve the simulation of DSL, and the striking negative bias for
375 the North Atlantic in CTRL is reduced. Compared with the traditional explicit eight tidal
376 constituents scheme, the new tidal scheme exhibits a latitudinal variation of DSL with a positive
377 difference in the tropics and a negative pattern in high latitudes, which improves the significant
378 positive bias of the Southern Ocean in CTRL.

379 It should be noted that the wave drag term formula proposed by Schiller and Fiedler (2007)
380 and the drag from internal wave generation (Jayne and Laurent, 2001; Simmons et al. 2004) are
381 adopted in the present study to decay the tidal energy, which is likely too strong in both tidal
382 experiments, especially with the traditional tidal forcing formula. Implementing a more
383 appropriate tidal drag parameterization in an OGCM still needs to be carried out. In addition, the

384 explicit introduction of tides into an OGCM is only a step towards upgrading ocean modeling. A
385 more detailed investigation into the impacts of the new tidal scheme on simulated ocean
386 circulations will be our future work, especially in an OCGM with a finer resolution and in a fully
387 coupled mode.

388 **Code availability.** *LICOM2.0 is the ocean component model of the Chinese Academy of Sciences*
389 *Earth System Model (CAS-ESM 2.0), which developed at IAP are intellectual property of IAP.*
390 *Permission to access the LICOM2.0 source code can be requested after contacting the*
391 *corresponding author (zqc@mail.iap.ac.cn) or Jiangbo Jin (jinjiangbo@mail.iap.ac.cn) and may*
392 *be granted after accepting the IAP Software License Agreement.*

393 **Data availability.** *TPXO9v2 is available from the following sources:*
394 *[https://doi.org/10.1175/1520-0426\(2002\)019<0183:EIMOBO>2.0.CO;2](https://doi.org/10.1175/1520-0426(2002)019<0183:EIMOBO>2.0.CO;2) (Egbert and Erofeeva,*
395 *2002). The station observations are from the sea level Data Assembly Center (DAC):*
396 *[https://doi.org/10.1175/1520-0426\(2001\)018<0077:AAOTTS>2.0.CO;2](https://doi.org/10.1175/1520-0426(2001)018<0077:AAOTTS>2.0.CO;2) (Ponchaut et al., 2001).*
397 *The observation of the DSL is available from the Archiving, Validation and Interpretation of*
398 *Satellite Oceanographic data (AVISO): <https://doi.org/10.5281/zenodo.5896655>.*

399 **Author contributions.** *QZ and JJ pondered the rationale of the method. JJ designed the*
400 *experiments. RG developed the model code and performed the simulations. JJ, MZ and RG*
401 *prepared the manuscript with contributions from all co-authors. MZ and GZ carried out*
402 *supervision.*

403 **Acknowledgments.** *This work is jointly supported by the National Natural Science Foundation of*
404 *China (Grant No 41991282), the Key Research Program of Frontier Sciences, the Chinese*
405 *Academy of Sciences (Grant No. ZDBS-LY-DQC010), the Strategic Priority Research Program*
406 *of the Chinese Academy of Sciences (Grant No. XDB42000000) and the open fund of the State*
407 *Key Laboratory of Satellite Ocean Environment Dynamics, Second Institute of Oceanography*
408 *(Grant No. QNHX2017). The simulations were performed on the supercomputers provided by the*
409 *Earth System Science Numerical Simulator Facility (EarthLab).*

REFERENCES

- 410
- 411 Arbic, B. K., Wallcraft, A. J., and Metzger, E. J.: Concurrent simulation of the eddy general
412 circulation and tides in a global ocean model, *Ocean Modell.*, 32(3–4), 175–187,
413 <https://doi.org/10.1016/j.ocemod.2010.01.007>, 2010.
- 414 [Boon, J.: *Secrets of the Tides*, Horwood Publishing, 2004.](#)
- 415 [Cartwright, D. E.: *Tides : a scientific history*, Cambridge University Press, 1999.](#)
- 416 Dong, X., Jin, J., Liu, H., Zhang, H., Zhang, M., Lin, P., Zeng, Q., Zhou, G., Yu, Y., Song, Lin,
417 M., Z., Lian, R., Gao, X., He, J., Zhang, D., and Chen, K.: CAS-ESM2.0 model datasets for
418 the CMIP6 Ocean Model Intercomparison Project Phase 1 (OMIP1), *Adv. Atmos. Sci.*, 38,
419 307–316, <https://doi.org/10.1007/s00376-020-0150-3>, 2021.
- 420 Egbert, G. D., and Erofeeva, S. Y.: Efficient Inverse Modeling of Barotropic Ocean Tides, *J.*
421 *Atmos. Ocean. Tech.*, 19(2), 183–204, [https://doi.org/10.1175/1520-](https://doi.org/10.1175/1520-0426(2002)019<0183:EIMOBO>2.0.CO;2)
422 [0426\(2002\)019<0183:EIMOBO>2.0.CO;2](https://doi.org/10.1175/1520-0426(2002)019<0183:EIMOBO>2.0.CO;2), 2002.
- 423 Egbert, G. D., and Ray, R. D.: Semi-diurnal and diurnal tidal dissipation from TOPEX/Poseidon
424 altimetry, *Geophys. Res. Lett.*, 30(17), 169–172, <https://doi.org/10.1029/2003GL017676>,
425 2003.
- 426 Fairall, C. W., Bradley, E. F., Hare, J. E., Grachev, A. A., and Edson, J. B.: Bulk
427 parameterization of air–sea fluxes: Updates and verification for the COARE algorithm, *J.*
428 *Climate*, 16, 571–591, 2003.

429 Gill, S.: Sea-level science: Understanding tides, surges, tsunamis and mean sea-level changes,
430 *Phys Today*, 68, 56–57, 2015.

431 Griffies, S. M., and Adcroft, A. J.: Formulating the Equations of Ocean Models, *J. Geophys. Res.*,
432 177, 281–317, <https://doi.org/10.1029/177GM18>, 2008.

433 [Griffies, S. M., Danabasoglu, G., Durack, P. J., Adcroft, A. J., Balaji, V., Böning, C. W.,](#)
434 [Chassignet, E. P., Curchitser, E., Deshayes, J., Drange, H., Fox-Kemper, B., Gleckler, P. J.,](#)
435 [Gregory, J. M., Haak, H., Hallberg, R. W., Heimbach, P., Hewitt, H. T., Holland, D. M.,](#)
436 [Ilyina, T., Jungclaus, J. H., Komuro, Y., Krasting, J. P., Large, W. G., Marsland, S. J.,](#)
437 [Masina, S., McDougall, T. J., Nurser, A. J. G., Orr, J. C., Pirani, A., Qiao, F., Stouffer, R. J.,](#)
438 [Taylor, K. E., Treguier, A. M., Tsujino, H., Uotila, P., Valdivieso, M., Wang, Q., Winton,](#)
439 [M., and Yeager, S. G.: OMIP contribution to CMIP6: experimental and diagnostic protocol](#)
440 [for the physical component of the Ocean Model Intercomparison Project, *Geosci. Model*](#)
441 [Dev.](#), 9, 3231–3296, <https://doi.org/10.5194/gmd-9-3231-2016>, 2016.

442 [Griffies, S. M., and Greatbatch, R. J.: Physical processes that impact the evolution of global](#)
443 [mean sea level in ocean climate models, *Ocean Modell.*, 51, 37–72,](#)
444 <https://doi.org/10.1016/j.ocemod.2012.04.003>, 2012.

445 Griffies, S. M., Harrison, M. J., Pacanowski, R. C., and Rosati, A.: A Technical Guide to MOM4,
446 GFDL Ocean group Tech. Rep, 5, 309–313, 2004.

447 Griffies, S. M., Schmidt, M., and Herzfeld, M.: Elements of mom4p1, GFDL Ocean Group Tech.
448 Rep, 6, 444.p, 2009.

449 Hendershott, M. C.: The effects of solid earth deformation on global ocean tides, *Geophys J Int*,
450 29(4), 389–402, <https://doi.org/10.1111/j.1365-246X.1972.tb06167.x>, 1972.

451 Huang, R. X.: Mixing and energetics of the oceanic thermohaline circulation, *J. Phys. Oceanogr.*,
452 29, 727–746, 1999.

453 Jayne, S. R. and Laurent, L. C. S.: Parameterizing tidal dissipation over rough topography,
454 *Geophys. Res. Lett.*, 28(5), 811–814, <https://doi.org/10.1029/2000GL012044>, 2001.

455 Jin, J. B., Zeng, Q. C., Wu, L., Liu, H. L., and Zhang, M. H.: Formulation of a new ocean salinity
456 boundary condition and impact on the simulated climate of an oceanic general circulation
457 model, *Sci. China Earth Sci.*, 60, 491–500, <https://doi.org/10.1007/s11430-016-9004-4>, 2017.

458 Jin, J. B., Zhang, H., Dong, X., Liu, H. L., Zhang, M. H., Gao, X., He, J. X., Chai, Z. Y., Zeng, Q.
459 C., Zhou, G. Q., Lin, Z. H., Yu, Y., Lin, P. F., Lian, R. X., Yu, Y. Q., Song, M. R., and
460 Zhang, D. L.: CAS-ESM2.0 model datasets for the CMIP6 Flux-Anomaly-Forced Model
461 Intercomparison Project (FAFMIP), *Adv. Atmos. Sci.*, 38(2), 296–306,
462 <https://doi.org/10.1007/s00376-020-0188-2>, 2021.

463 Killworth, P. D., Stainforth, D., Webb, D. J., and Paterson, S. M.: The development of a free-
464 surface Bryan–Cox–Semtner ocean model, *J. Phys. Oceanogr.*, 21, 1333–1348, 1991.

465 Large, W. G., and Yeager, S.: Diurnal to decadal global forcing for ocean and sea-ice models:
466 the datasets and flux climatologies, NCAR Technical Note (No. NCAR/TN-460+STR),
467 <https://doi.org/10.5065/D6KK98Q6>, 2004.

468 Laurent, L. C. St., Simmons, H. L., and Jayne, S. R.: Estimating tidally driven mixing in the deep
469 ocean, *Geophys. Res. Lett.*, 29(23), 211–214, <https://doi.org/10.1029/2002GL015633>, 2002.

470 Liu, H. L., Lin, P. F., Yu, Y. Q., and Zhang, X. H.: The baseline evaluation of LASG/IAP
471 climate system ocean model (LICOM) version 2, *Acta Meteorol. Sin.*, 26, 318–329,
472 <https://doi.org/10.1007/s13351-012-0305-y>, 2012.

473 MacKinnon, J.: Mountain waves in the deep ocean, *Nature*, 501, 321–322,
474 <https://doi.org/10.1038/501321a>, 2013.

475 Melet, A., Hallberg, R., Legg, S., and Polzin, K.: Sensitivity of the ocean state to the vertical
476 distribution of internal-tide driven mixing, *J. Phys. Oceanogr.*, 43(3), 602–615,
477 <https://doi.org/10.1175/JPO-D-12-055.1>, 2013.

478 Montenbruck, and Gill.: Sun and moon, *Satellite Orbits: Models, Methods and Applications*, 69–
479 77, 2000.

480 Munk, W. and Wunsch, C.: Abyssal recipes II: energetics of tidal and wind mixing, *Deep Sea*
481 *Res. Part I Oceanogr. Res. Pap.*, 45(12), 1977–2010, [https://doi.org/10.1016/S0967-](https://doi.org/10.1016/S0967-0637(98)00070-3)
482 [0637\(98\)00070-3](https://doi.org/10.1016/S0967-0637(98)00070-3), 1998.

483 Müller, M., Haak, H., Jungclaus, J. H., Sündermann, J., and Thomas, M.: The effect of ocean
484 tides on a climate model simulation, *Ocean Modell.*, 35(4), 304–313,
485 <https://doi.org/10.1016/j.ocemod.2010.09.001>, 2010.

486 Ponchaut, F., Lyard, F., and Provost, C. L.: An analysis of the tidal signal in the WOCE sea level
487 dataset, *J. Atmos. Ocean. Tech.*, 18(1), 77–91, [https://doi.org/10.1175/1520-](https://doi.org/10.1175/1520-0426(2001)018<0077:AAOTTS>2.0.CO;2)
488 0426(2001)018<0077:AAOTTS>2.0.CO;2, 2001.

489 Postlethwaite, C. F., Morales Maqueda, M. A., le Fouest, V., Tattersall, G. R., Holt, J. T., and
490 Willmott, A. J.: The effect of tides on dense water formation in Arctic shelf seas, *Ocean Sci.*,
491 7, 203–217, <https://doi.org/10.5194/os-7-203-2011>, 2011.

492 Saenko, O. A. and Merryfield, W. J.: On the effect of topographically enhanced mixing on the
493 global ocean circulation, *J. Phys. Oceanogr.*, 35, 826–834, 2005.

494 [Sakamoto, K., Tsujino, H., Nakano, H., Hirabara, M., and Yamanaka, G.: A practical scheme to](#)
495 [introduce explicit tidal forcing into an OGCM, *Ocean Sci.*, 9, 1089–1108,](#)
496 <https://doi.org/10.5194/os-9-1089-2013>, 2013.

497 Schiller, A.: Effects of explicit tidal forcing in an OGCM on the water-mass structure and
498 circulation in the Indonesian throughflow region, *Ocean Modell.*, 6(1), 31–49,
499 [https://doi.org/10.1016/S1463-5003\(02\)00057-4](https://doi.org/10.1016/S1463-5003(02)00057-4), 2004.

500 Schiller, A., and Fiedler, R.: Explicit tidal forcing in an ocean general circulation model,
501 *Geophys. Res. Lett.*, 34(3), L03611, <https://doi.org/10.1029/2006GL028363>, 2007.

502 Schneider, D. P., Deser, C., Fasullo, J., and Trenberth, K. E.: Climate data guide spurs discovery
503 and understanding, *Eos Trans. AGU*, 94(13), 121, <https://doi.org/10.1002/2013EO130001>,
504 2013.

505 Schwiderski, E.: On charting global ocean tides, *Rev. Geophys.*, 18(1), 243–268,
506 <https://doi.org/10.1029/RG018i001p00243>, 1980.

507 Shriver, J. F., Arbic, B. K., Richman, J. G., Ray, R. D., Metzger, E. J., Wallcraft, A. J., and
508 Timko, P. G.: An evaluation of the barotropic and internal tides in a high-resolution global
509 ocean circulation model, *J. Geophys. Res.*, 117, C10024,
510 <https://doi.org/10.1029/2012JC008170>, 2012.

511 Shum, C. K., Woodworth, P. L., Andersen, O. B., Egbert, G. D., Francis, O., King, C., Klosko, S.
512 M., Provost, C. L., Li, X., Molines, J. M., Parke, M. E., Ray, R. D., Schlax, M. G., Stammer,
513 D., Tierney, C. C., Vincent, P., and Wunsch, C. I.: Accuracy assessment of recent ocean tide
514 models, *J. Geophys. Res.*, 102(C11), 25173–25194, <https://doi.org/10.1029/97JC00445>,
515 1997.

516 Simmons, H. L., Jayne, S. R., Laurent, L. C. S., and Weaver, A. J.: Tidally driven mixing in a
517 numerical model of the ocean generalcirculation, *Ocean Modell.*, 6, 245–263,
518 [https://doi.org/10.1016/S1463-5003\(03\)00011-8](https://doi.org/10.1016/S1463-5003(03)00011-8), 2004.

519 Thomas, M., Sündermann, J., and Maier-Reimer, E.: Consideration of ocean tides in an OGCM
520 and impacts on subseasonal to decadal polar motion excitation, *Geophys. Res. Lett.*, 28(12),
521 2457–2460, <https://doi.org/10.1029/2000GL012234>, 2001.

522 Wahr, J. M. and Sasao, T.: A diurnal resonance in the ocean tide and in the earth load response
523 due to the resonant free “core nutation”, *Geophys. J. Int.*, 64(3), 747–765,
524 <https://doi.org/10.1111/j.1365-246X.1981.tb02693.x>, 1981.

525 Wang, X., Liu, Z., and Peng, S.: Impact of tidal mixing on water mass transformation and
526 circulation in the south china sea, *J. Phys. Oceanogr.*, 47(2), 419–432,
527 <https://doi.org/10.1175/JPO-D-16-0171.1>, 2017.

528 Wilmes, S. B., Schmittner, A., and Green, J. A. M.: Glacial Ice Sheet Extent Effects on Modeled
529 Tidal Mixing and the Global Overturning Circulation, *Paleoceanogr. Paleoclimatol.*, 34,
530 1437–1454, <https://doi.org/10.1029/2019PA003644>, 2019.

531 Wunsch, C., and Ferrari, R.: Vertical mixing, energy, and the general circulation of the oceans,
532 *Annu. Rev. Fluid Mech.*, 36, 281–314, 2004.

533 Yu, Y., Liu, H., and Lan, J.: The influence of explicit tidal forcing in a climate ocean circulation
534 model, *Acta Meteorol. Sin.*, 35(9), 42–50, <https://doi.org/10.1007/s13131-016-0931-9>, 2016.

535 Yu, Z., Liu, H., and Lin, P.: A Numerical Study of the Influence of Tidal Mixing on Atlantic
536 Meridional Overturning Circulation (AMOC) Simulation, *Chinese J. Atmospheric Sci.*,
537 41(5), 1087–1100, 2017.

538 Zhang, H., Zhang, M., Jin, J., Fei, K., Ji, D., Wu, C., Zhu, J., He, J., Chai, Z., Xie, J., Dong, X.,
539 Zhang, D., Bi, X., Cao, H., Chen, H., Chen, K., Chen, X., Gao, X., Hao, H., Jiang, J., Kong,
540 X., Li, S., Li, Y., Lin, P., Lin, Z., Liu, H., Liu, X., Shi, Y., Song, M., Wang, H., Wang, T.,
541 Wang, X., Wang, Z., Wei, Y., Wu, B., Xie, Z., Xu, Y., Yu, Y., Yuan, L., Zeng, Q., Zeng, X.,
542 Zhao, S., Zhou, G., Zhu, J.: Description and climate simulation performance of CAS-ESM
543 version 2, *J. Adv. Model. Earth. Sy.*, 12, e2020MS002210,
544 <https://doi.org/10.1029/2020MS002210>, 2020.

- 545 Zhang, R. H., and Endoh, M.: A free surface general circulation model for the tropical Pacific
546 Ocean, *J. Geophys. Res.*, 97(C7), 11237–11255, <https://doi.org/10.1029/92JC00911>, 1992.
- 547 Zhang, X., and Liang, X.: A numerical world ocean general circulation model. *Adv. Atmos. Sci.*,
548 6(1), 44–61, 1989.
- 549 Zhou, X. B., Zhang, Y. T., and Zeng, Q. C.: The interface wave of thermocline excited by the
550 principal tidal constituents in the Bohai Sea, *Acta Meteorol. Sin.*, 24(2), 20–29, 2002.

551 **Figure Captions**

552 **Figure 1.** Schematic of the tidal forces generated by the Moon, where M_m , a , D_m , and L are the
553 Moon, the radius of the Earth, the distance to the Moon, and the distance of the Moon from any
554 point X on the Earth, respectively. θ_m is the zenith angle of point X relative to the Moon, and r is
555 the angle between the Moon pointing to the center of the Earth and point X.

556

557 **Figure 2.** Spatial patterns of the spring tides for Exp1 (the first column) and Exp2 (the second
558 columns), and the interval between the row is six hours. The units are cm.

559

560 **Figure 3.** Spatial patterns of the neap tides for Exp1 (the first column) and Exp2 (the second
561 columns), and the interval between the row is six hours. The units are cm.

562

563 **Figure 4.** Spatial patterns of the amplitude and phase of K1 for (a) the observation (Obs), (b)
564 Exp1, (c) Exp2, (d) the total error for Exp1, (e) the total error for Exp2, and (f) the difference in
565 error between Exp2 and Exp1. The observation is from TPXO9v2 (Egbert and Erofeeva, 2002).
566 The units are cm, and the lines of the constant phase are plotted every 45° in black.

567

568 **Figure 5.** The contributions to the total error of K1 resulting from errors in (a) tidal amplitude
569 and (b) phase for Exp1; (c) and (d) are the same as above, but for Exp2. The units are cm.

570

571 **Figure 6.** Spatial patterns of the amplitude and phase of M2 for (a) the observation (Obs), (b)
572 Exp1, (c) Exp2, (d) the total error for Exp1, (e) the total error for Exp2, and (f) the difference in
573 error between Exp2 and Exp1. The observation is from TPXO9v2 (Egbert and Erofeeva, 2002).
574 The units are cm, and the lines of the constant phase are plotted every 45° in black.

575

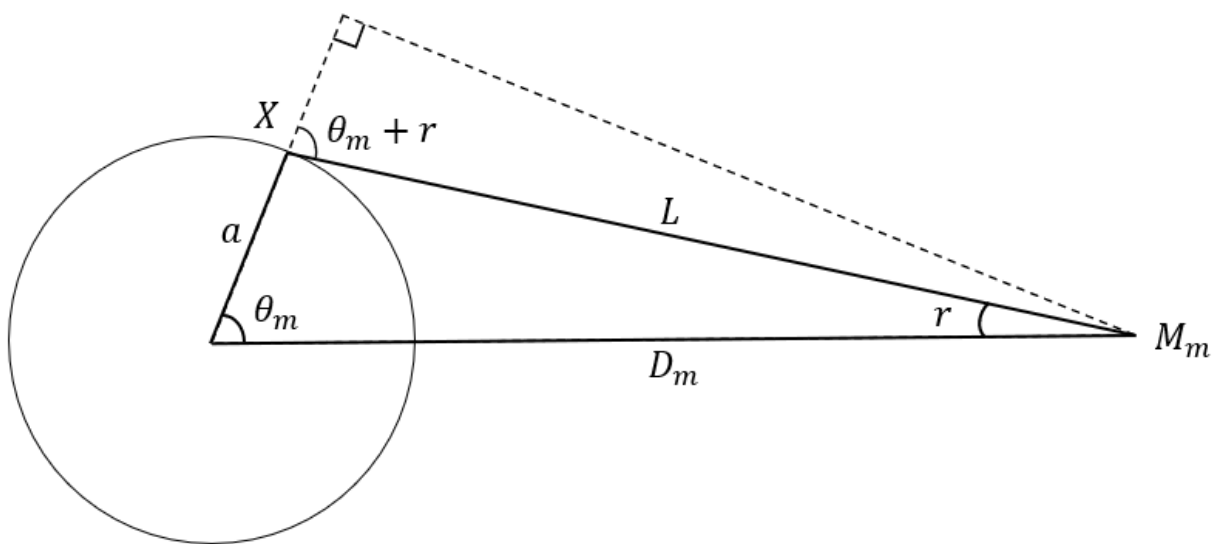
576 **Figure 7.** The contributions to the total error of M2 resulting from errors in (a) tidal amplitude
577 and (b) phase for Exp1; (c) and (d) are the same as above, but for Exp2. The units are cm.

578

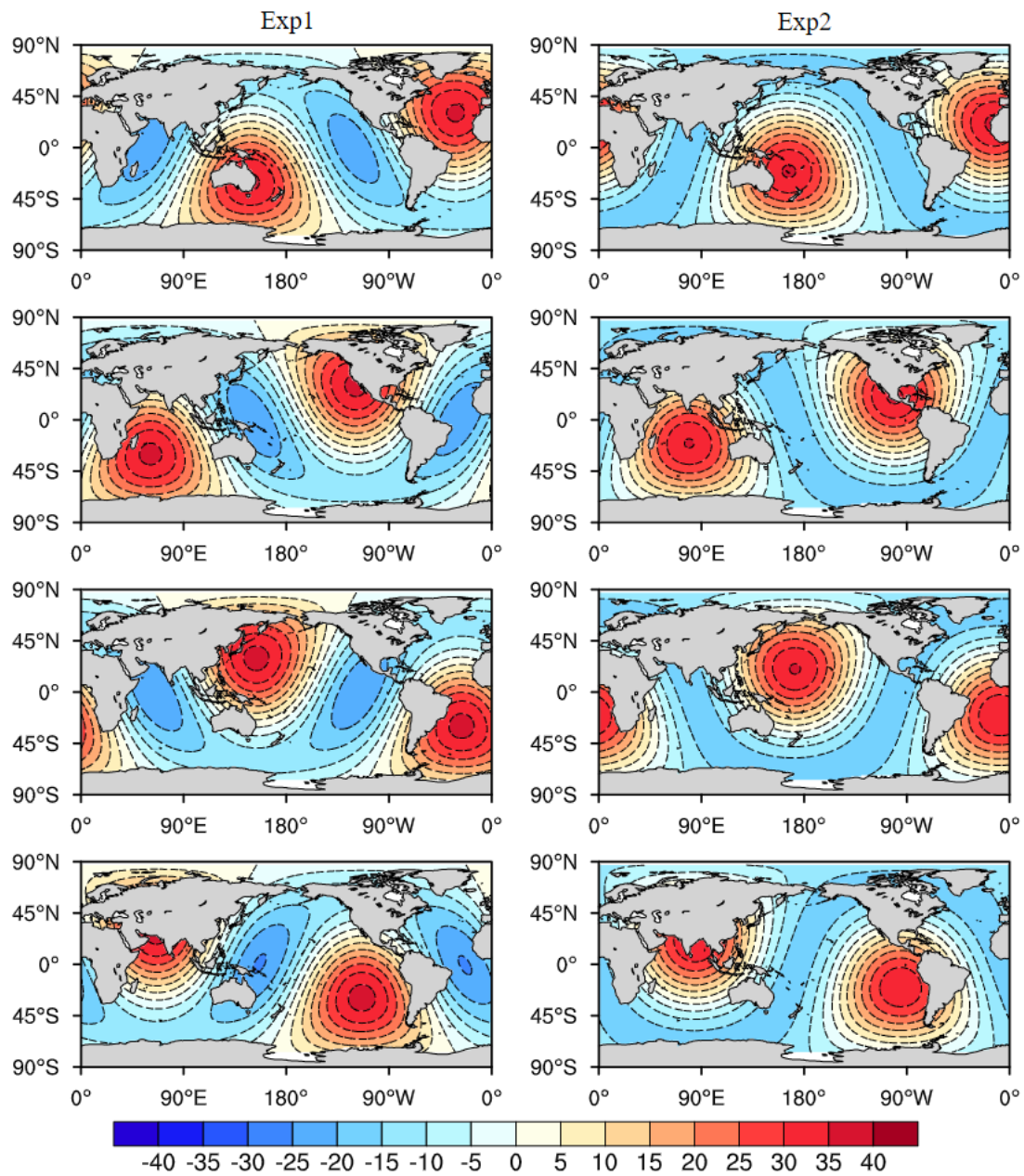
579 **Figure 8.** Spectrum analysis of sea surface height for (a) the observation (Obs), (b) Exp1, and (c)
580 Exp2, and (d–f) is the same as above. The observation is from WOCE (Ponchaut et al., 2001).
581 The upper panels are for the Diego Ramirez Islands (56.56°S, 68.67°W) and the lower panels are
582 for Yakutat (59.54°N, 139.73°W).

583

584 **Figure 9.** Spatial patterns of the dynamic sea level for (a) the observation (Obs), (b) CTRL, (c)
585 the difference between CTRL and observation, (d) the difference between Exp1 and CTRL, (e)
586 the difference between Exp2 and CTRL, and (f) the difference between Exp2 and Exp1. The
587 observation is from AVISO (Schneider et al., 2013), and the units are m.



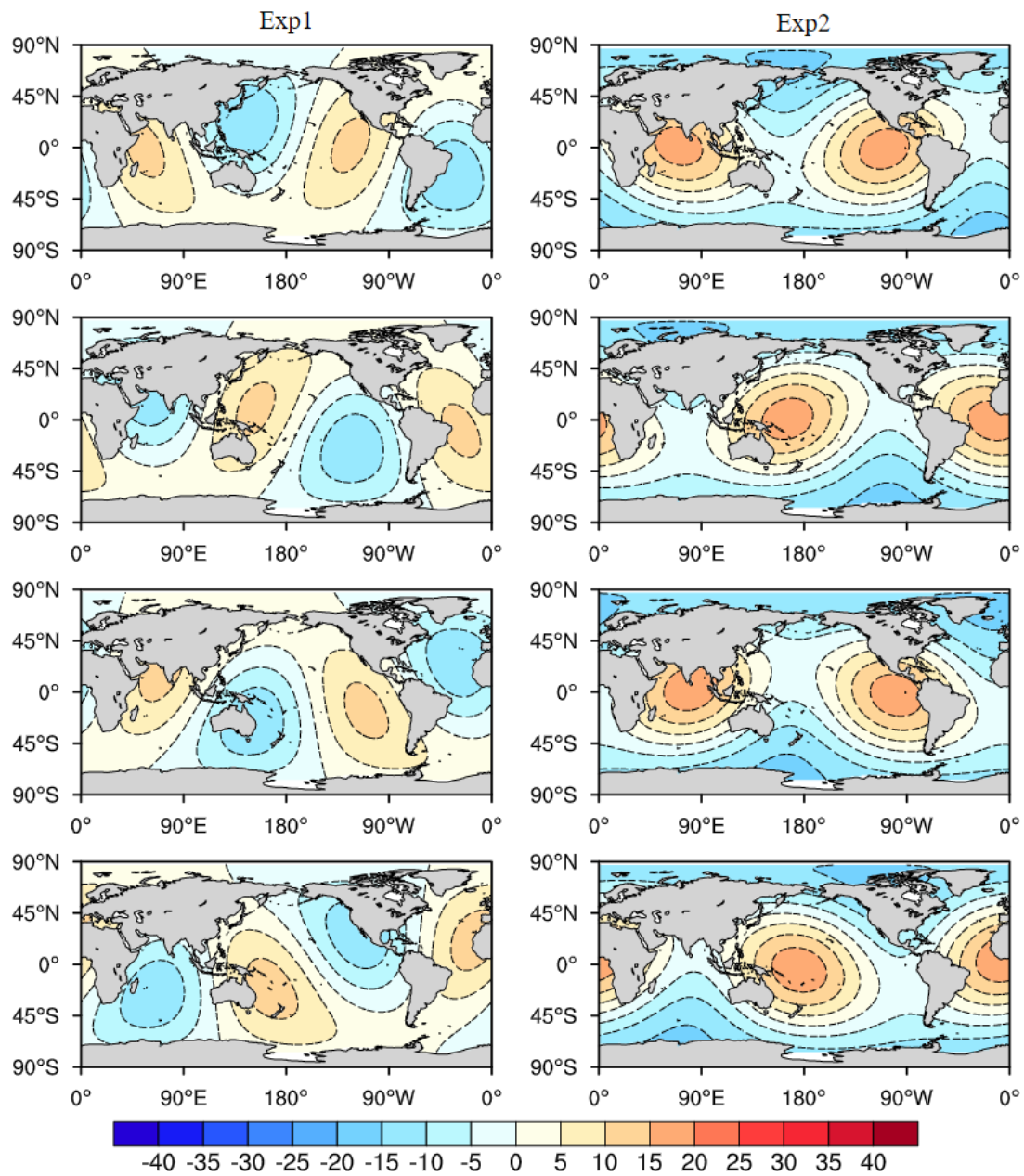
588
 589 **Figure 1.** Schematic of the tidal forces generated by the Moon, where M_m , a , D_m , and L are the
 590 Moon, the radius of the Earth, the distance to the Moon, and the distance of the Moon from any
 591 point X on the Earth, respectively. θ_m is the zenith angle of point X relative to the Moon, and r is
 592 the angle between the Moon pointing to the center of the Earth and point X.



593

594 **Figure 2.** Spatial patterns of the spring tides for Exp1 (the first column) and Exp2 (the second

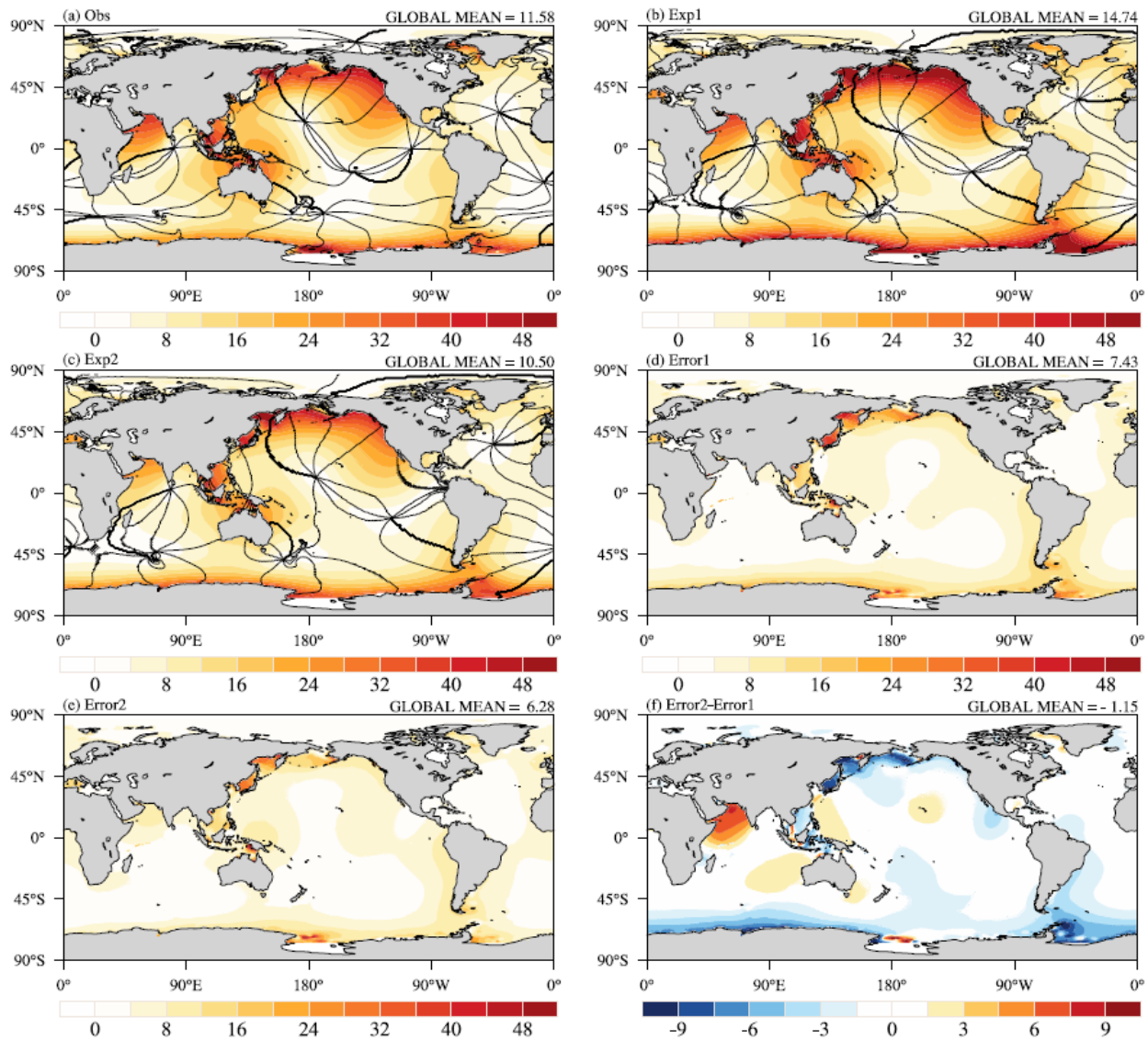
595 columns), and the interval between the row is six hours. The units are cm.



596

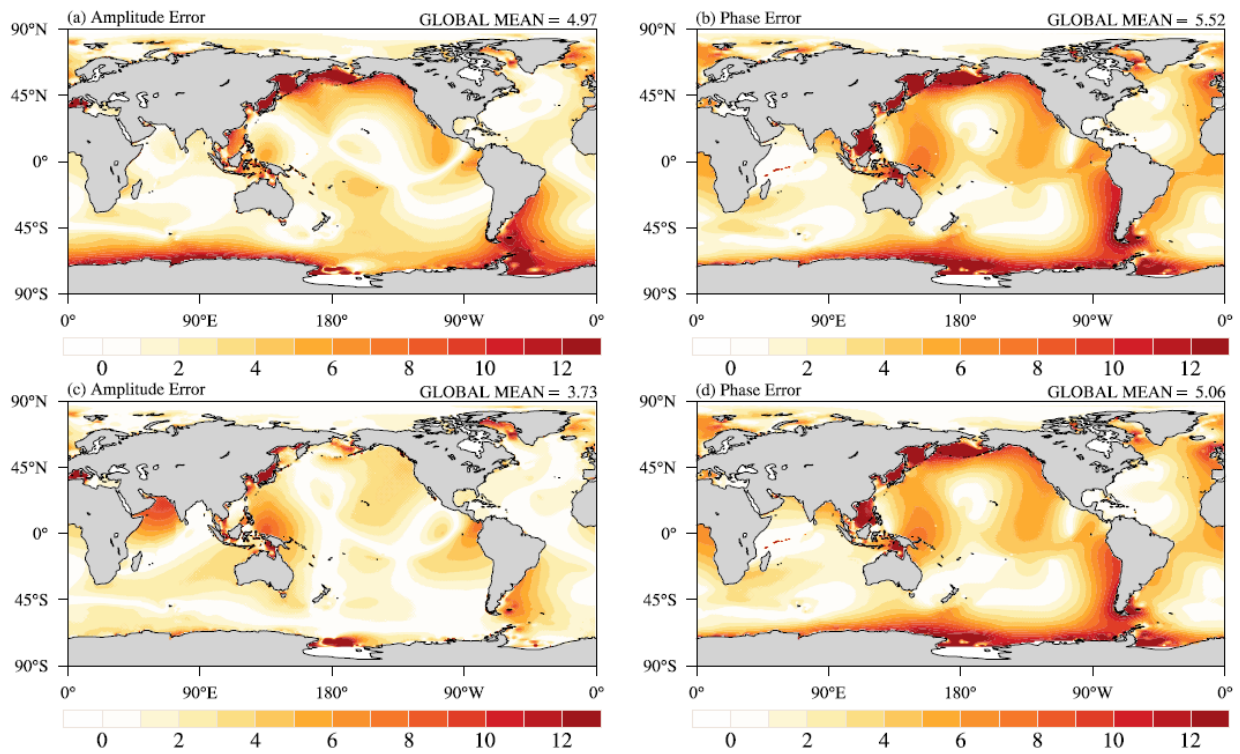
597 **Figure 3.** Spatial patterns of the neap tides for Exp1 (the first column) and Exp2 (the second

598 columns), and the interval between the row is six hours. The units are cm.



599

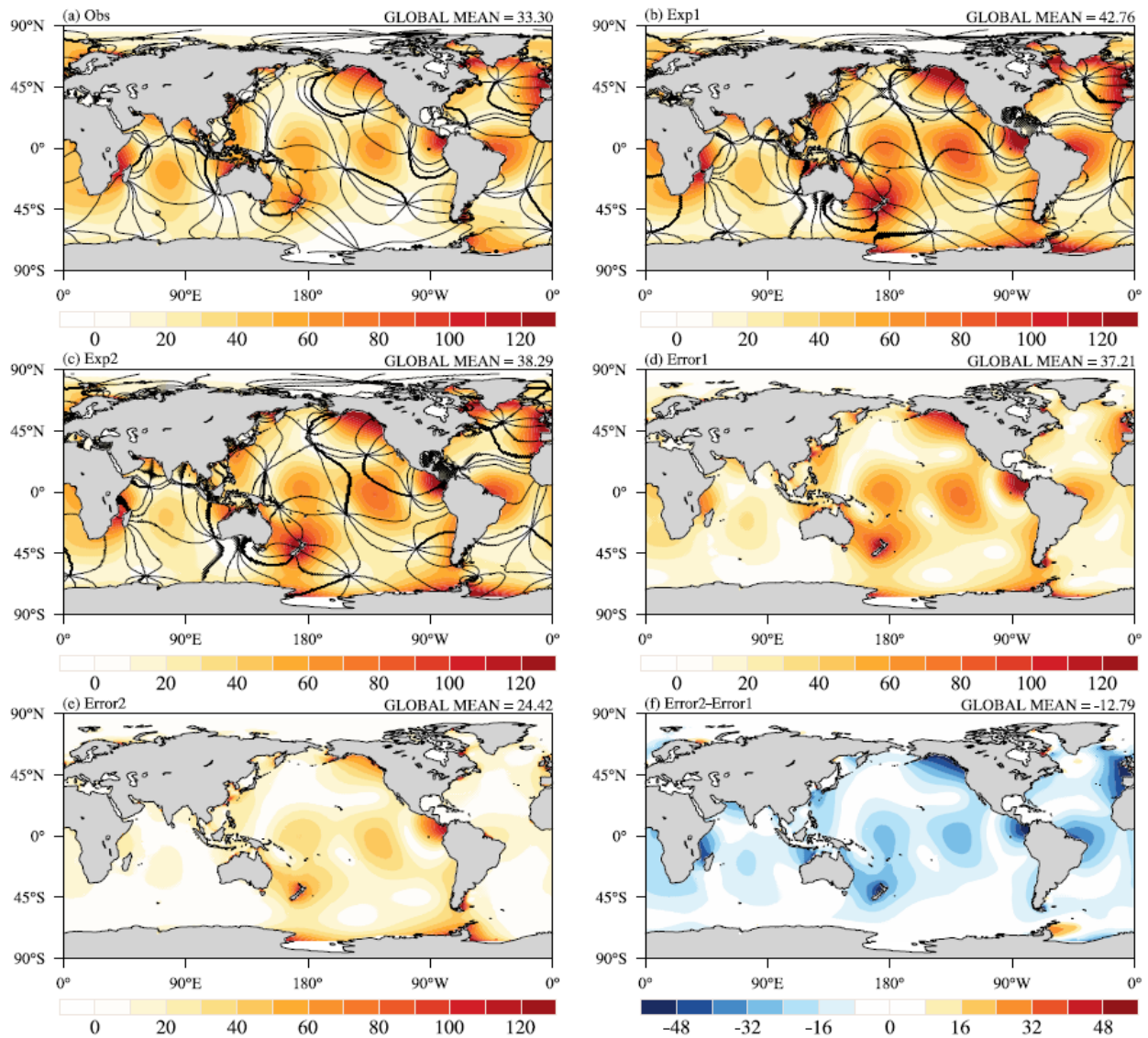
600 **Figure 4.** Spatial patterns of the amplitude and phase of K1 for (a) the observation (Obs), (b)
 601 Exp1, (c) Exp2, (d) the total error for Exp1, (e) the total error for Exp2, and (f) the difference in
 602 error between Exp2 and Exp1. The observation is from TPXO9v2 (Egbert and Erofeeva, 2002).
 603 The units are cm, and the lines of the constant phase are plotted every 45° in black.



604

605 **Figure 5.** The contributions to the total error of K1 resulting from errors in (a) tidal amplitude

606 and (b) phase for Exp1; (c) and (d) are the same as above, but for Exp2. The units are cm.



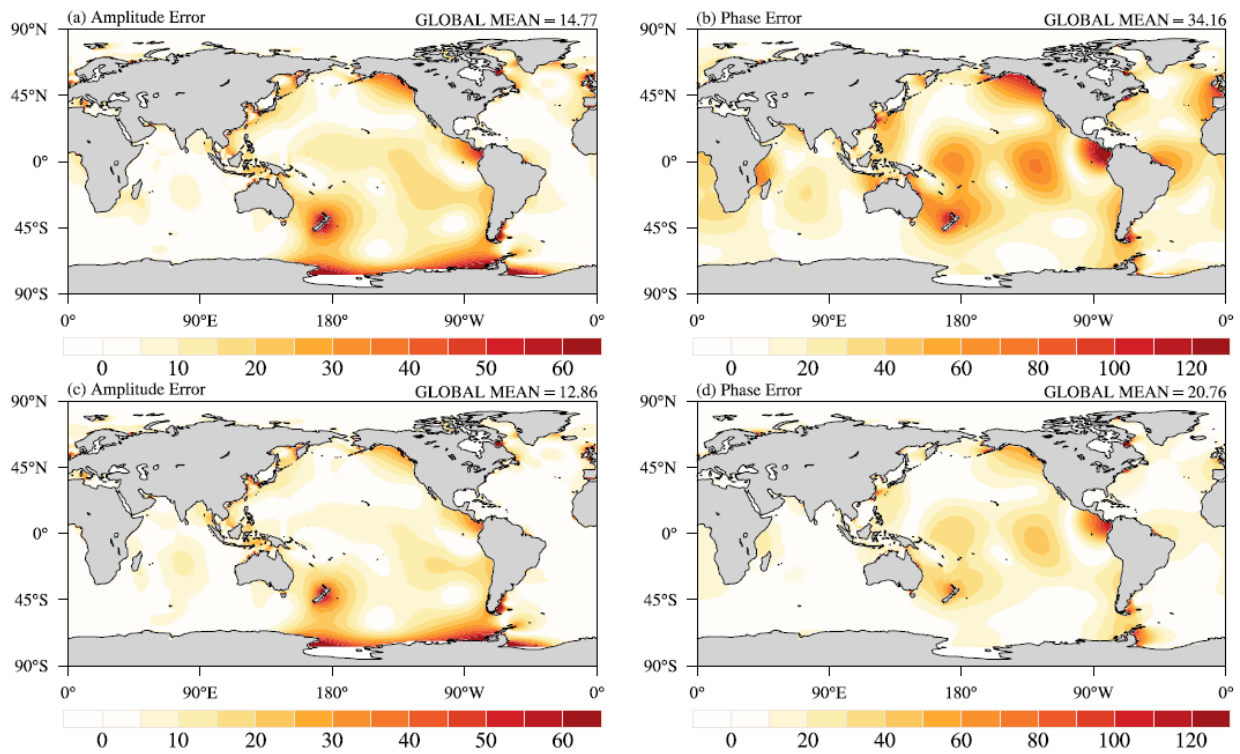
607

608 **Figure 6.** Spatial patterns of the amplitude and phase of M2 for (a) the observation (Obs), (b)

609 Exp1, (c) Exp2, (d) the total error for Exp1, (e) the total error for Exp2, and (f) the difference in

610 error between Exp2 and Exp1. The observation is from TPXO9v2 (Egbert and Erofeeva, 2002).

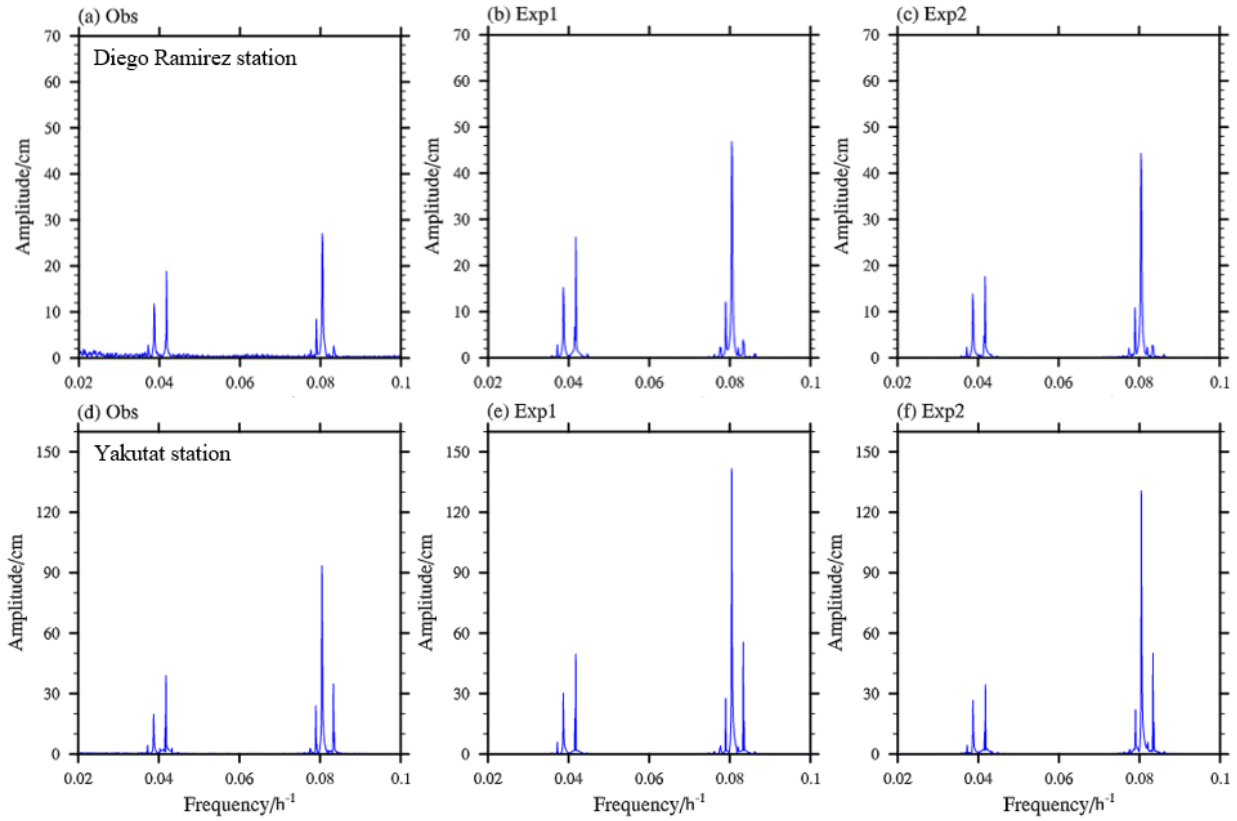
611 The units are cm, and the lines of the constant phase are plotted every 45° in black.



612

613 **Figure 7.** The contributions to the total error of M2 resulting from errors in (a) tidal amplitude

614 and (b) phase for Exp1; (c) and (d) are the same as above, but for Exp2. The units are cm.



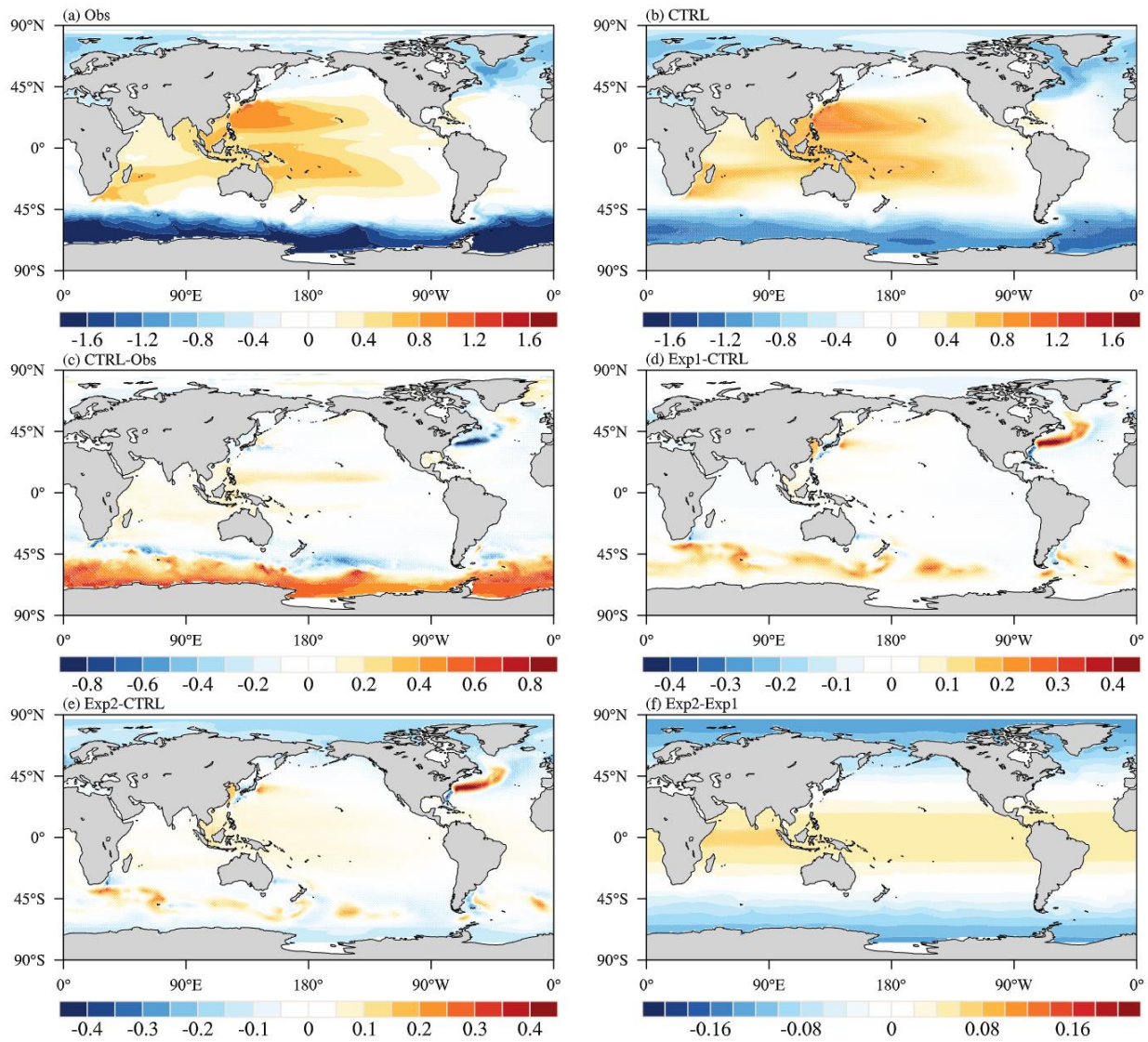
615

616 **Figure 8.** Spectrum analysis of sea surface height for (a) the observation (Obs), (b) Exp1, and (c)

617 Exp2, and (d–f) is the same as above. The observation is from WOCE (Ponchaut et al., 2001).

618 The upper panels are for the Diego Ramirez Islands (56.56°S, 68.67°W) and the lower panels are

619 for Yakutat (59.54°N, 139.73°W).



620

621

Figure 9. Spatial patterns of the dynamic sea level for (a) the observation (Obs), (b) CTRL, (c)

622

the difference between CTRL and observation, (d) the difference between Exp1 and CTRL, (e)

623

the difference between Exp2 and CTRL, and (f) the difference between Exp2 and Exp1. The

624

observation is from AVISO (Schneider et al., 2013), and the units are m.

625

626 **Table Captions**

627 **Table 1.** Global mean values of the amplitudes of the eight tidal constituents during observation,
628 Exp1 and Exp2, and the amplitude, phase, and total errors of the eight tidal constituents in Exp1
629 and Exp2. The units are cm. The better amplitude and lower errors in Exp2 relative to Exp1 are
630 marked by bold font.

631

632 **Table 2.** The amplitudes of the eight tidal constituents during the observation (Obs), Exp1 and
633 Exp2 at the Diego Ramirez Islands (56.56°S, 68.67°W) and Yakutat (59.54°N, 139.73°W). The
634 observation is from WOCE (Ponchaut et al., 2001), and the units are cm. The better amplitude in
635 Exp2 relative to Exp1 is marked by bold font.

636

637 **Table 1.** Global mean values of the amplitudes of the eight tidal constituents during observation,
638 Exp1 and Exp2, and the amplitude, phase, and total errors of the eight tidal constituents in Exp1
639 and Exp2. The units are cm. The better amplitude and lower errors in Exp2 relative to Exp1 are
640 marked by bold font.

	Global mean			Amplitude Error		Phase Error		Total Error	
	Obs	Exp1	Exp2	Exp1	Exp2	Exp1	Exp2	Exp1	Exp2
M2	33.30	42.76	38.29	14.77	12.86	34.16	20.76	37.21	24.42
S2	13.35	12.45	9.85	5.11	5.68	10.04	7.49	11.26	9.40
N2	7.08	7.74	9.79	2.20	3.34	5.41	5.88	5.84	6.76
K2	3.75	10.89	7.33	6.50	3.72	8.01	5.39	10.32	6.55
K1	11.58	14.74	10.50	4.97	3.73	5.52	5.06	7.43	6.28
O1	8.34	10.59	9.79	3.28	3.16	8.26	4.30	8.89	5.34
P1	3.62	13.49	9.47	9.18	5.58	2.57	2.84	9.53	6.26
Q1	1.76	1.62	2.19	0.57	0.76	1.16	1.26	1.29	1.47

641 **Table 2.** The amplitudes of the eight tidal constituents during the observation (Obs), Exp1 and
 642 Exp2 at the Diego Ramirez Islands (56.56°S, 68.67°W) and Yakutat (59.54°N, 139.73°W). The
 643 observation is from WOCE (Ponchaut et al., 2001), and the units are cm. The better amplitude in
 644 Exp2 relative to Exp1 is marked by bold font.

	Diego Ramirez			Yakubu		
	Obs	Exp1	Exp2	Obs	Exp1	Exp2
M2	27.01	46.84	44.28	101.24	141.58	130.65
S2	2.62	3.93	2.73	35.61	55.49	50.05
N2	8.49	12.10	10.84	24.48	27.71	22.04
K2	1.15	2.94	2.12	9.34	16.28	15.71
K1	18.82	26.13	17.59	39.33	49.53	34.37
O1	11.73	15.20	13.83	20.53	30.18	26.55
P1	3.75	6.66	4.80	11.94	17.70	11.05
Q1	2.82	2.81	2.28	2.79	5.96	4.37

645